Electrostatics and optimal arrangement of ionic triangular lattices confined to cylindrical fibers

Kevin L. Kohlstedt,[1,2] Graziano Vernizzi,[1,*] and Monica Olvera de la Cruz[1,2]
[1]*Department of Materials Science, Northwestern University, Evanston, Illinois 60208, USA*
[2]*Department of Chemical Engineering, Northwestern University, Evanston, Illinois 60208, USA*
(Received 12 August 2009; published 30 November 2009)

We study the optimal packing of triangular ionic lattices on the surface of nanofibers. We compute the favored orientation of the lattice with respect to the axis of the cylindrical fiber, and we determine the effects of the surface curvature. Electrostatic interactions prefer chiral arrangements only for special families of lattices that depend on the fiber diameter. However, there are families of lattices that energetically promote achiral configurations. Besides the long-range Coulomb interactions we consider the behavior of short-range elastic forces, represented by interconnected springs between neighboring ions. In this case a different family of achiral lattices is always preferred. We also show that varying the stoichiometric composition of charges, as well as including higher-order curvature effects, does not significantly modify such a scenario.

DOI: 10.1103/PhysRevE.80.051503 PACS number(s): 82.70.−y, 81.16.Rf, 68.35.Gy, 62.23.St

I. INTRODUCTION

A fundamental question still exists on what the origin of asymmetry is in biological molecules [1]. Pasteur, in his famous letter in 1874 [2,3], attributed the apparently omnipresent asymmetry in biological systems to more fundamental asymmetries of cosmic order ("L'univers est dissymétrique"). Yet today it is unclear what the mediator of these asymmetries is, especially those that operate within the thermal energy landscape of biological organisms (i.e., not kinetically arrested). Even though a majority of biological molecules and assemblies are known to be asymmetric, no complete theory has been put forth describing anisotropic assemblies ubiquitous in biology from chiral assemblies to helical surface patterns. Broken symmetries such as mirror symmetry or chirality (i.e., breaking of mirror symmetry) are known to be essential in the generation of functional molecules [4]. Some examples include fibrillar [5,6] and spherical viruses [7], specific directional growth of a extracellular molecules [8,9], de novo peptide nanotubes [10,11], and synthetic design of biologically inspired supramolecular systems [12,13].

Ionic pair interactions have been shown to be an essential element in complex assemblies seen in biomolecular systems such as F-actin [14], spherical viruses [15], and amyloid fibril aggregation [16]. The interplay between surface charges and the surface curvature can lead to several phenomena being observed, such as faceting [17,18], chirality [19,20], and other packing arrangements [21] including charged nanopatterns [22,23]. Our aim here is to elucidate what effect long-range Coulomb interactions have on an ionic lattice wrapped around cylindrical fibers—the simplest of curved surfaces. The model we propose compares a variety achiral and chiral lattices confined to cylindrical geometry and describes how chirality spontaneously arises for some energetically favorable configurations but, surprisingly, not all. The model may be useful for describing an emergent chiral angle due to arrangements of metallic multivalent ions condensed along double stranded DNA known to have strong interactions with specific DNA groups [24–26]. More directly, we are interested in describing ionic lattice configurations tiled on nanoscale fibers. An important example is the surface forces between adsorbed charged molecules on carbon nanotubes. An understanding of the structure of the adsorbed charges is sought here, though competing anisotropic interactions such as hydrogen bonding and π-π stacking could also be important in determining the chiral structure as well [27–29].

We recently conjectured that chirality can arise at the nanoscale from the competition of Coulomb and short-range interactions on a cylindrical surface [20]. In particular, we described how a lamellar pattern of opposite charged domains on a cylindrical surface prefers chiral arrangements. Interestingly, even without a competing short-range interaction (described as a line tension), charged stripes on a oppositely charged cylindrical surface prefer helical configurations [30].

Lamellar patterns are a one-dimensional lattice wrapped around the nanofiber. In this paper we consider the more general case of full two-dimensional lattices wrapped around a cylinder (see Fig. 1). Specifically we address the question whether electrostatic interactions on a cylinder favor again chiral arrangements for an ionic assembly. By doing so, one has to take into account that the cylindrical geometry imposes strong commensurability constraints on the two-dimensional lattice, requiring any possible arrangement to be uniquely labeled by a pair of integer numbers (known also as "chiral indices" in connection with carbon nanotubes [31,32]). However, in order to make a correct and unbiased comparison between the energies of chiral and achiral configurations at a given fiber radius, we organize all possible lattice arrangements into suitable "families," each family being characterized by a fixed value of the radius. We discuss how electrostatics govern the energetics among family members and favor chiral arrangements only for a special class of families. Our results show that the interplay between electrostatics and chirality for a two-dimensional ionic lattice is quite different from its one-dimensional counterpart, that is, striped patterns. In particular, we report evidence that the commensurability constraints effectively inhibit the preferen-

*Corresponding author: g-vernizzi@northwestern.edu

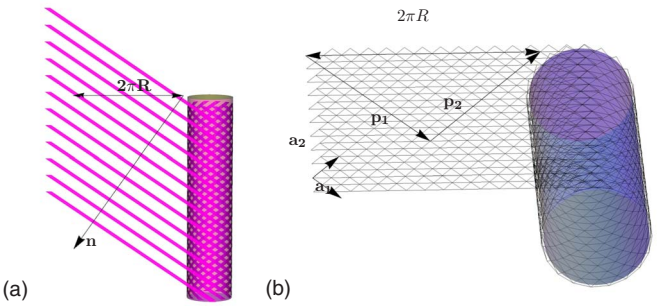

FIG. 1. (Color online) On the left: a one-dimensional lamellar lattice, with lattice index n, has a *continuous* set of chiral angles [30]. In other words, the commensurability constraint of the lamellar lattice $2\pi R\cos\omega = nL$ yields one-parameter solutions $R(\omega)$. On the right: a two-dimensional lattice, with lattice indices (p_1,p_2), when wrapped around a cylinder determines completely both the radius R and the chiral angle ω. The details of the commensurability constraints are discussed in Sec. II.

tial chiral angle found in the less restricted case of striped patterns on fibers [20].

In this work we study also the effect of short-range strain forces over chiral and achiral families. We find that in all cases strain interactions lead to achiral configurations, which are however different from the ones obtained by pure electrostatic interactions. We therefore analyze the instability that arises when combining the two competing effects. The connection between strain and electrostatic interactions in tethered ionic curved surfaces has since long drawn the attention of the physics community [33]. We analyze here both electrostatics and strain energy effects on an ionic lattice enveloping a cylindrical geometry. In planar two-dimensional systems already such a competition leads to a variety of behaviors and complex phases [34]. Similarly, strain-mediated systems on films have long been of interest for application to semiconductor films [35,36] and to magnetic systems [37]. In films of binary alloys the competition between macroscopic phase segregation and strain field is responsible for the formation of nanopatterns [38]. Binary mixtures layered on a substrate may generate strains between the two lattices. They are a promising tool for designing new functional nanoscale materials due to their nanopatterning capacity [39].

We organize the paper in the following manner. Section II describes the model we use to calculate the electrostatic energy of a lattice on a cylinder. We present the results in Sec. III for the cases of triangular ionic lattices at 2:1 or 3:1 stoichiometric ratio. Next, in Sec. IV we compare our results with the ones from a purely elastic model. We also show how higher-order curvature corrections do not affect our results substantially. Finally, in Sec. V we comment on possible applications, limitations, and extensions of our findings.

II. MODEL

A. Cylindrical geometry and constraints

Any lattice on a cylindrical surface can be promptly mapped onto a two-dimensional periodic plane $\{x,z\}$ by using cylindrical coordinates (the $\hat{\mathbf{z}}$ direction coinciding with the axis of the cylinder and the $\hat{\mathbf{x}}$ direction being periodic with $2\pi R$ period). We assume that such a "unwrapped" lattice is a regular planar lattice, with lattice vectors $\mathbf{a}_1$, $\mathbf{a}_2$, lattice angle γ, and a tilt (chiral) angle ω between $\mathbf{a}_1$ and $\hat{\mathbf{x}}$ (see Fig. 2). The geometrical description of a lattice wrapped around a cylinder has been widely used in the area of carbon nanotubes when describing hexagonal graphene lattices [40]. There, the requirement of commensurability of the lattice with the cylindrical geometry has been shown to lead naturally to the definition of two lattice chiral indices (p_1,p_2) [31,32] that completely characterize the carbon nanotube. In this section we report similar formulas for the generic case of an oblique lattice since such a case will be used in Sec. IV.

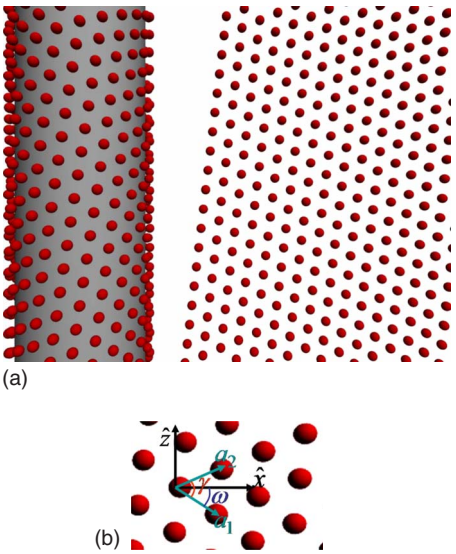

FIG. 2. (Color online) A lattice on a cylinder can be projected on a periodic plane. The lattice vectors on the plane are $(\mathbf{a}_1,\mathbf{a}_2)$, with lattice angle γ. We define the chiral angle ω as the angle between $\mathbf{a}_1$ and the direction $\hat{\mathbf{x}}$ orthogonal to the cylinder axis and tangent to the cylinder surface.

Due to the cylindrical geometry, the lattice must be commensurate when navigating on a circumferential path, that is, the vector $\mathbf{C}=\{0,2\pi R\}$ must belong to the lattice. As a consequence, there exists two integer numbers (p_1,p_2), the chiral indices, such that $\mathbf{C}=p_1\mathbf{a}_1+p_2\mathbf{a}_2$. By writing the commensurability constraint for each component along x and z, with $\mathbf{a}_1=a_1\{\cos\omega,-\sin\omega\}$ and $\mathbf{a}_2=a_2\{\cos(\gamma-\omega),\sin(\gamma-\omega)\}$ (see Fig. 2), we obtain two equations that can be solved with respect R and ω,

$$R_{p_1,p_2}=\frac{\sqrt{T}}{2\pi},\quad T=a_1^2p_1^2+a_2^2p_2^2+2a_1a_2p_1p_2\cos\gamma, \tag{1}$$

$$\omega_{p_1,p_2}=\arccos\left(\frac{a_1p_1+a_2p_2\cos\gamma}{\sqrt{T}}\right), \tag{2}$$

and T is the "triangulation number." Both the cylinder radius R_{p_1,p_2} and chiral angle ω_{p_1,p_2} are uniquely identified by the pair (p_1,p_2). It is straightforward to verify that in the case of

regular ($a_1=a_2\equiv a$) triangular lattice ($\gamma=\frac{\pi}{3}$) the equations simplify to

$$R_{p_1,p_2}=\frac{a\sqrt{p_1^2+p_1p_2+p_2^2}}{2\pi},$$

$$\omega_{p_1,p_2}=\arccos\left(\frac{2p_1+p_2}{2\sqrt{p_1^2+p_1p_2+p_2^2}}\right), \tag{3}$$

and for square lattice $\gamma=\frac{\pi}{2}$,

$$R_{p_1,p_2}=\frac{a\sqrt{p_1^2+p_2^2}}{2\pi},$$

$$\omega_{p_1,p_2}=\arccos\left(\frac{p_1}{\sqrt{p_1^2+p_2^2}}\right). \tag{4}$$

In such two cases, the lattice acquires a periodicity also in the z direction, that is, it becomes invariant under translations $z\rightarrow z+P$: for the triangular case, $P=an_2\sqrt{3}/(2\cos\omega)$ and n_1, n_2 are uniquely determined by $n_1/n_2=-p_2/p_1$ such that they are prime with respect each other; for the square lattice case, $P=an_2/\cos\omega$ and n_1, n_2 are uniquely determined by $n_1/n_2=-(p_1+2p_2)/(2p_1+p_2)$ such that they are prime with respect to each other [32].

The reciprocal lattice $\mathbf{Q}$, which will be used in Sec. II B and it is defined by $\mathbf{Q}\cdot\mathbf{\Lambda}=2\pi m$ for all lattice vectors $\mathbf{\Lambda}$, has components $\mathbf{Q}=\{q_x,q_z\}$ given by

$$q_x=\frac{m_1p_1+m_2p_2}{R}, \tag{5}$$

$$q_z=\frac{(m_2p_1-m_1p_2)\csc\gamma+(m_2p_2-m_1p_1)\cot\gamma}{R}. \tag{6}$$

We note that in the reciprocal space the commensurability condition $q_xR=m_1p_1+m_2p_2$ is independent of γ.

When considering a lattice with a basis, as in the cases for 2:1 or 3:1 stoichiometric ratio of charges (see Fig. 3), the unit cell is defined by the sublattice of positive charges only, while the negative ones form the basis. Let α be the distance between a positive charge and a neighboring negative one, then $a=\sqrt{3}\alpha$ for the 2:1 case, and $a=2\alpha$ for the 3:1 case. For the rest of this paper we will take $\alpha=1$ as the unit of length.

We note that the model described in this section has the feature that the lattice can be wrapped on cylinders with different radii R while a is kept constant as if the nodes of the lattice were "glued" over the cylindrical surface at fixed arc-length distances. Later in this paper we will discuss a more accurate model where the lattice bonds are fixed through three-dimensional chords of the cylinder, which provides corrections of order $O(1/R^2)$ to the geometrical arrangement of the lattice.

B. Electrostatic energy

In this section we show how the electrostatic energy of a cylindrical two-dimensional ionic lattice can be computed by the standard Ewald summation method [41]. We assume that

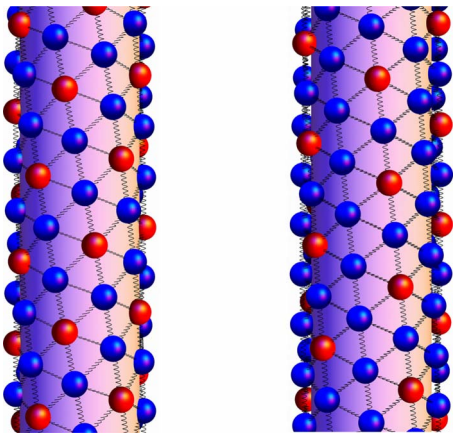

FIG. 3. (Color online) Triangular ionic lattices at 2:1 (on the left) or 3:1 (on the right) stoichiometric ratios. The arrangement of charges is different due to unit-cell electroneutrality constraint. The blue (dark gray) spheres represent negative (−1) charges, while the red (light gray) spheres represent positive (+2) and (+3) charges on the left and on the right, respectively.

all charges have the same size, which reflects the choice of fixing the nearest-neighbor distance equal to $\alpha=1$. Obviously, the cylindrical geometry allows the covering lattice to be regular and without defects, therefore each charge is connected with six (or four) nearest-neighbor charges. The electrostatic interaction of the charges is assumed simply to be the Coulomb potential. We could have used a different potential, such as a screened Yukawa potential [20]. Although it has been shown in [30] that chiral configurations can arise spontaneously both from long-range and screened Coulomb interactions only when the inverse screening length ξ and the lattice constant a are such that $\xi a<1$, for simplicity we use only a Coulomb potential. We impose a global electroneutrality constraint, and as mentioned above we consider two possible cases: a triangular lattice of charges at 2:1 or 3:1 stoichiometric ratio (see Fig. 3). We begin by writing the electrostatic energy of a two-dimensional ionic lattice,

$$E_{lattice}=\frac{1}{2}{\sum_{i,j}}' q_iq_jV_{ij}, \tag{7}$$

where q_i is the charge at the ith site and $\Sigma'_{i,j}$ conveniently stands for the double sum with $i\neq j$. The three-dimensional long-range Coulomb potential is

$$V_{ij}=\frac{1}{4\pi\varepsilon}\frac{1}{D_{ij}}, \tag{8}$$

with ε being the homogeneous dielectric constant of the space outside and inside the cylinder and D_{ij} being the three-dimensional distance (through cords of the cylinder) between ions on the lattice,

$$D_{ij}=\sqrt{4R^2\sin^2\frac{x_j-x_i}{2R}+(z_j-z_i)^2}. \tag{9}$$

In our notation, the position $\mathbf{p}_i=\{R\cos\theta,R\sin\theta,z\}$ of the ith ion is written in cylindrical coordinates, and the angles are parametrized by the arc length $x=\theta R$. This is precisely

the parametrization that maps a three-dimensional problem into a two-dimensional one. As done in Sec. II A, the initial cylindrical ionic lattice is mapped onto a two-dimensional plane $\{x,z\}$, periodic along the x direction with periodicity $2\pi R$. Let $\mathbf{b}_i$ be the basis vectors that describe positions of negative ions inside an electroneutral Wigner cell, with lattice vectors $\mathbf{a}_1$, $\mathbf{a}_2$. Then, any vector of the lattice has the form $\mathbf{\Lambda}+\mathbf{b}_i$, with $\mathbf{\Lambda}=n_1\mathbf{a}_1+n_2\mathbf{a}_2$. Since the total electrostatic energy $E_{lattice}$ diverges for an infinite lattice, we consider the finite energy *per cell* E_{cell} by setting $E_{lattice}=E_{cell}N_{cell}$ (where N_{cell} is the number of cells),

$$E_{cell}=\frac{1}{8\pi\varepsilon}\sum_{\mathbf{\Lambda},\mathbf{b}_i,\mathbf{b}_j}{}'\frac{q_iq_j}{D_{ij}}\theta(2\pi R-\|x_i-x_j\|). \tag{10}$$

The distance D_{ij} is between a charge at position $\mathbf{b}_i$ in the unit cell and a charge at position $\mathbf{\Lambda}+\mathbf{b}_j$ on the lattice and Σ' includes the condition $D_{ij}\neq 0$.

We can now employ the standard Ewald summation method [41] to efficiently calculate E_{cell}. We replace $1/D_{ij}$ in Eq. (10) with the Gaussian integral representation $2/\sqrt{\pi}\int_0^\infty dte^{-t^2D_{ij}^2}$ and subsequently split the integral into a long-range part and short-range part,

$$E_{cell}=\frac{1}{4\pi^{3/2}\varepsilon}\sum_{\mathbf{\Lambda},\mathbf{b}_i,\mathbf{b}_j}{}'q_iq_j\left[\int_0^\eta dt+\int_\eta^\infty dt\right]e^{-t^2D_{ij}^2}. \tag{11}$$

Similar to Ref. [20], the long-range term of Eq. (11) is written in the reciprocal space using the Poisson summation formula. The resulting expression is

$$E_{cell}=\frac{1}{4\pi^{3/2}\varepsilon}\frac{1}{A_c}\sum_{\mathbf{Q}}\hat{q}(\mathbf{Q})\hat{q}(-\mathbf{Q})\hat{f}(\mathbf{Q})-\frac{1}{4\pi^{3/2}\varepsilon}\sum_i q_i^2\eta$$
$$+\frac{1}{4\pi^{3/2}\varepsilon}\sum_{\mathbf{\Lambda},\mathbf{b}_i,\mathbf{b}_j}{}'q_iq_j\int_\eta^\infty dte^{-t^2D_{ij}^2}, \tag{12}$$

where $A_c=\mathbf{a}_1\times\mathbf{a}_2$ is the area of the unit cell and the Fourier transforms $\hat{f}(\mathbf{Q})$ and $\hat{q}(\mathbf{Q})$ are given by

$$\hat{f}(\mathbf{Q})=\int_{\mathbb{R}^2}d^2\mathbf{p}e^{-i\mathbf{Q}\cdot\mathbf{p}}\int_0^\eta dte^{-t^2D_{ij}^2}, \tag{13}$$

$$\hat{q}(\mathbf{Q})=\sum_{i\in cell}q_ie^{-i\mathbf{b}_i\cdot\mathbf{Q}}. \tag{14}$$

Equation (11) is independent of η, thus its value is often fixed by requiring that the two sums over the real space and over the reciprocal space have the same rate of convergence. In Eq. (13), the two-dimensional vector $\mathbf{p}=(x,z)$ is bounded by the cylinder with $x\epsilon[0,2\pi R]$ and $z\epsilon\mathbb{R}$. The first term in Eq. (12) accounts for the long-range energy, while the second term subtracts the $D=0$ case from the first term. The two-dimensional integral in Eq. (13) is evaluated exactly,

$$\hat{f}(\mathbf{Q})=R\pi^{3/2}\int_0^{2R^2\eta^2}\frac{dt}{t}e^{-t-q_z^2R^2/(2t)}I_{q_xR}(t), \tag{15}$$

where the function $I_n(z)$ is the modified Bessel function of the first kind. Due to the lack of a closed form for $\hat{f}(\mathbf{Q})$ and for the lattice sums in Eq. (12), we evaluate E_{cell} numerically. We choose the value of η in a region where E_{cell} is independent of η, i.e., $\partial E_{cell}/\partial\eta\approx 0$ [42]. We include a number of elements in the sums adaptively by requiring that the numerical precision is of the order of 10^{-8}.

III. RESULTS

In order to establish whether a cylindrical ionic lattice spontaneously adopts chiral arrangements, we need to compare the electrostatic energy of achiral configurations versus chiral ones, having the same fiber radius R. We remind here that all lengths are measured in unit of α, which is the arc-length distance between a pair of positive-negative neighboring charges (see Fig. 3), and it is therefore kept fixed throughout this section. Moreover, we characterize the chirality of a configuration by the value of the chiral angle ω of the sublattice composed by the positive charges only. Accordingly, it is easy to verify that the only possible achiral configurations for a 2:1 or 3:1 triangular ionic lattice are at $\omega=0$ and $\omega=\frac{\pi}{6}$ [we limit $0\leq\omega\leq\frac{\pi}{6}$ since $E_{cell}(\omega+\frac{\pi}{6})=E_{cell}(\frac{\pi}{6}-\omega)$ and E_{cell} is periodic with period $\frac{\pi}{3}$]. Any other configuration with $\omega\neq 0$ and $\omega\neq\frac{\pi}{6}$ is chiral.

At this point it is important to notice that due to the commensurability constraints not all values of the radius R correspond to degenerate achiral and/or chiral lattices. In order to make a rational comparison we have grouped lattices into families that contain both achiral and chiral configurations at the same value of the radius. Namely, since all possible chiral angles ω_{p_1,p_2} and radii R_{p_1,p_2} are parameterized by the two chiral indices (p_1,p_2), we first build a set of *all* (p_1,p_2) values such that each pair in a set corresponds to the same R_{p_1,p_2}. For simplicity, we limit to the case $p_1\geq p_2$ since $T_{p_1,p_2}=T_{p_2,p_1}$ and the electrostatic energy of right-handed configurations is always equal to the electrostatic energy of its left-handed counterpart. Such a choice does not decrease the generality of our arguments. Equation (1) states that $R\propto\sqrt{T}$, and therefore a family $\mathcal{F}_T$ contains all pairs (p_1,p_2) corresponding to the same triangulation number T. We call *degenerate pairs*, any two pairs that belong to the same family. From Eq. (3) the pairs that correspond to achiral lattices are of the form $(p,0)$ or (p,p), and they can be called "armchair" or "zigzag," respectively [40] (see Fig. 4).

For instance, in the case of a regular triangular lattice, where $T=p_1^2+p_2^2+p_1p_2$, the family $\mathcal{F}_{49}=\{(7,0),(5,3)\}$ contains two configurations: one is chiral (5,3,) and the other is achiral (7,0). Another example is the family $\mathcal{F}_{21}=\{(4,1)\}$ which contains only one chiral configuration, and it is not possible to find other configurations with the same T, i.e., having the same fiber radius. Also the family $\mathcal{F}_{91}=\{(9,1),(6,5)\}$ has two elements, both chiral. From these examples it is evident that when we order the families according to their T values, we should keep only degenerate families that contain one achiral configuration and at least an achiral one. That is so because in order to establish whether electrostatics favor chiral versus achiral lattices (at a given radius R), we have to include achiral and chiral configurations in comparison. Otherwise the symmetry breaking

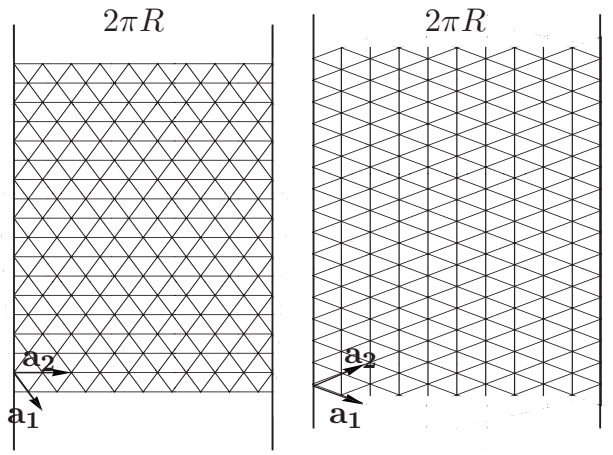

FIG. 4. There are two achiral triangular lattices on the cylinder: the armchair (left) and zigzag (right). They have chiral indices $(p,0)$ and (p,p), respectively. Our notation is only apparently the opposite of the one commonly used for carbon nanotubes, where armchair configurations are of type (p,p) and zigzag configurations are of type $(p,0)$. However, in those cases the lattice is hexagonal, which is dual to the triangular lattices we consider here.

would be explicit and a consequence of the commensurability constraints solely, not of electrostatics. Moreover, it is straightforward to verify that it is impossible to have a pair of chiral indices that are degenerate with both armchair $(p,0)$ and zigzag (p,p) configurations. Thus all the families we consider belong to two main classes: the class of families $\mathcal{F}^{\square}$ that contain armchair configurations and the class $\mathcal{F}^{\diamond}$ containing zigzag configurations. For instance, when doing the energy comparison for the above examples, we would not consider the family $\mathcal{F}_{21}$ since it contains only one elements and cannot be used for testing, and we would also exclude the family $\mathcal{F}_{91}$ since it does not contain any achiral family. However the family $\mathcal{F}_{49}$ satisfies the requirements, and in fact it belongs to the class $\mathcal{F}^{\square}$ containing armchair configurations. In the Appendix we report tables of the elements of the families $\mathcal{F}^{\square}$ and $\mathcal{F}^{\diamond}$ for all $T<10^4$, both for triangular cylindrical lattices and for square cylindrical lattices.

We evaluate E_{cell} from Eqs. (12), (14), and (15) for all possible pairs of chiral indices (p_1,p_2) with $0\leq p_2\leq p_1 \leq 100$. Through direct comparison of the numerical values of E_{cell} within the members of each family, we determine whether the lattice over the cylinder prefers to be chiral or not. Our results for the 2:1 stoichiometric case are summarized in Fig. 5, where all possible pairs of chiral indices (p_1,p_2) are represented as dots in the plane $\{\omega,E\}$. For the sake of completeness, we evaluated the electrostatic energy also for all the nondegenerate configurations. The configurations that are degenerate are joined by a line, thus visually identifying all members within a given family (i.e., fibers at fixed radius). The "crowding" of lines at the top of the figure is a consequence of the fact that by increasing p_1 and p_2, the radius increases rapidly. The corresponding energy quickly tends to the value of the Madelung energy for a planar ionic lattice, which in the case of a 2:1 stoichiometric ratio is $E_{2:1}\simeq -4.6265$. For clarification, we show in Fig. 6 a magnified version of the lower part of Fig. 5, that is in the region

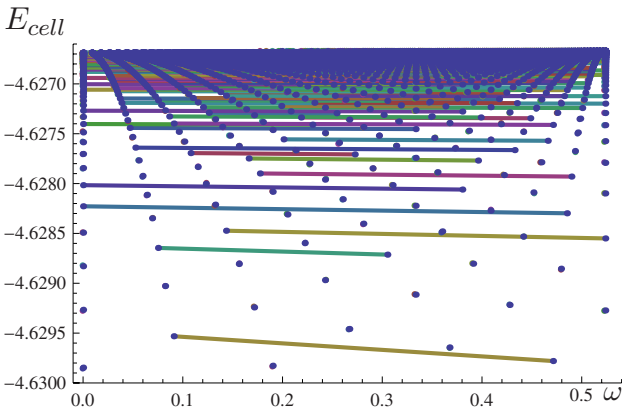

FIG. 5. (Color online) In this plot, each dot represents a (p_1,p_2) configuration with $0\leq p_2\leq p_1\leq 100$, in the plane $\{\omega,E\}$, for a triangular ionic lattice at 2:1 stoichiometric ratio. The lines join configurations that belong to the same family (i.e., they can be wrapped on cylinders with the same radius).

at small radii. The values of the pairs (p_1,p_2) are explicitly indicated. All the armchair configurations of type $(p,0)$ correspond to $\omega=0$ while all the zigzag configurations of type (p,p) correspond to $\omega=\pi/6$. All other configurations are chiral. One can clearly see the three types of families we mentioned above: the first type is the one with families made of a single element, and as such they are not useful for addressing the issue of chiral instability. The second type is one of the families having two or more elements, but no achiral elements of type $(p,0)$ or (p,p). The third type is given by families that are degenerate with either armchair $(p,0)$ or zigzag (p,p) and never with both since that would be impossible. A common feature of all families with degenerate elements is that configurations with larger ω have lower energy. In other words all the lines have negative slope. We verified this fact for all the configurations in Fig. 5. The main consequence of this finding is that the lowest-energy configuration for families of type $\mathcal{F}^{\diamond}$ is achiral zigzag configuration [i.e., of type (p,p)], whereas the lowest-energy configuration for families of type $\mathcal{F}^{\square}$ is *chiral* [i.e., of type $(p,0)$]. This means that long-range electrostatic interactions can induce spontaneous chirality of cylindrical ionic lattices depending on the

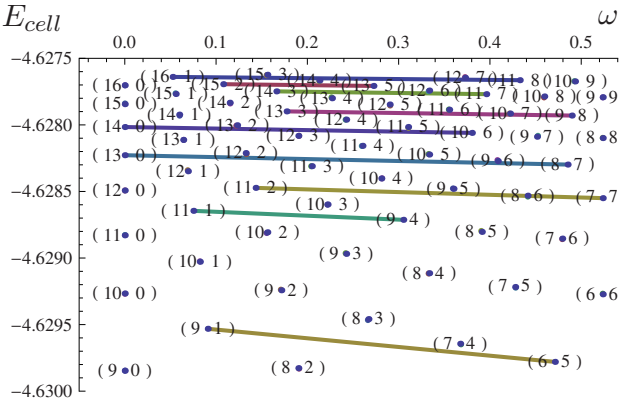

FIG. 6. (Color online) This figure is a magnification of the lower region of the diagram in Fig. 5. For clarity, the configurations are labeled by their chiral indices (p_1,p_2).

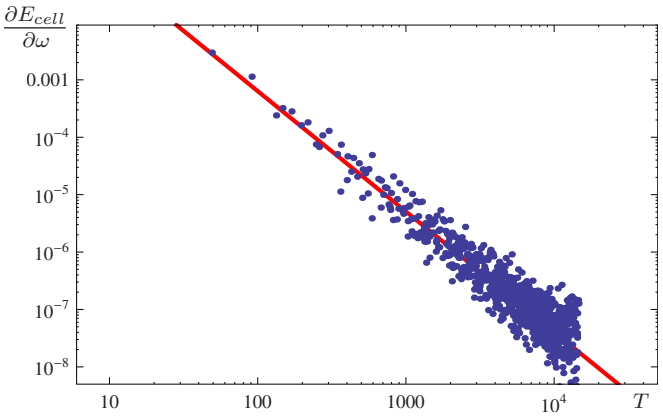

FIG. 7. (Color online) $\partial E_{cell}/\partial\omega$ is plotted on logarithmic scales versus the triangulation number T for the 2:1 ionic ratio. The power-law fitting $E'_{cell}(\omega) \sim T^{\gamma}$ (solid line) gives a scaling exponent of $\gamma = -2.09 \pm 0.03$. The radius R scale with T as $R \sim \sqrt{T}$.

value of the radius. However, as the radius increases also the number of elements in each family $\mathcal{F}^{\square}$ increases, with chiral angles that are closer and closer to $\pi/6$ (but never equal). Therefore, such special chiral configurations are relevant at small R. Furthermore, at large radii the system quickly converges toward an isotropic planar ionic lattice. That is why the slope of the lines in Figs. 5 and 6 goes to zero at large radii. Such a behavior follows a power law, as we show in Fig. 7. The slopes $\partial E_{cell}/\partial\omega$ are computed for each family $\mathcal{F}_T$ containing at least two elements, and they are plotted versus the triangulation number T of that family. For the case of 2:1 stoichiometric ratio we find $\partial E_{cell}/\partial\omega \sim R^{-4}$. Analogously, we verified that $E_{cell} \sim R^{-2}$ up to subleading logarithmic corrections. This is consistent with an achiral term at the order $O(R^{-2})$ in the large-R asymptotics.

We also find that the results for the 3:1 case are completely similar to the one for the 2:1 case. The only difference is a shift in the value of the energies due to a different value of the Madelung constant at large R, which is $E_{3:1} \simeq -8.42$. Such a shift does not alter the fact that an ionic lattices at 3:1 stoichiometric ratio prefers to adopt zigzag (p,p) configurations when the commensurability constraints allow it. For those reasons we do not reproduce here the plots for the 3:1 case, being qualitatively identical to the 2:1 case.

For a 1:1 square ionic lattice, we found again a behavior completely similar to the 2:1 case, with the only difference that the energy minima at zigzag configurations (p,p) are at an angle $\omega = \pi/4$ and the Madelung energy at large R is $E_{1:1} \simeq = -1.615$.

IV. DISCUSSION

The main result of Sec. III is that electrostatics can still favor chiral configurations but not in all cases. Whether the energy is the lowest for chiral or achiral structures, it all depends on the specific value of the fiber radius R. If R is such that its family contains zigzag configurations, then the lowest energy is a zigzag configuration. If however R is such that the family belongs to the armchair configuration, then the lowest energy is a chiral configuration. Furthermore, in case there are several chiral configurations that are degenerate with a armchair achiral configuration, the configuration with the largest chiral angle (i.e., closer to $\pi/6$) is the preferred one. We do not find much qualitative difference between the 2:1 or 3:1 ionic lattice, and besides an expected energy shift, they behave identically.

These results are interesting because they are substantially different from the effect of electrostatics on a lattice of charged stripes around the cylinder [20,30]. In fact, in the latter case, which is effectively a one-dimensional lattice, not only electrostatics yield chiral configurations but also a "universal" chiral limit angle $\omega^* = \arccos\sqrt{3/5}$ appears at large R. In the present two-dimensional case however chirality is not always preferred, and even when it does the chiral angle seems to go to $\pi/6$ at large R.

We posit here a possible explanation for such a different behavior. The strong influence that the family class type (i.e., the cylinder radius) has on the chiral or achiral fate of the ionic lattice and the discrete discontinuous nature of the two-dimensional system indicates that the main responsibility for such a behavior is from the commensurability constraints. As we mentioned above, both the radius R_{p_1,p_2} and the chiral angle ω_{p_1,p_2} assume values over a discrete set and not over a continuous interval as it occurs for the one-dimensional case. In [20], it has been shown that the large-R asymptotic expansion of the Fourier transform of the Coulomb potential has a minimum at $\omega = \omega^*$. This mathematical fact is independent from the particular chosen distribution of charges over the cylinder. The minima of Eq. (7) at large R generally depend on both the functional form of the potential and the specific chosen surface charge distribution. However the minimization in the one-dimensional case for striped cylindrical patterns is over a continuous set [the single commensurability constraint $2\pi R \cos\omega = nL$ has a one-parameter family of solutions $R(\omega)$], while in the two-dimensional case the minimization is over a discrete set of points (i.e., over the members of each family). In the latter case, the minima of $E_{lattice}$ cannot freely "fall" onto the minima of the Coulomb potential (in the reciprocal space) because of the discreteness of the configuration space due to the strong commensurability constraints. When R is large, the commensurability constraints vanish gradually, but the discrete nature of the space of possible configurations remains, and the two nonintersecting classes of families $\mathcal{F}^{\diamond}$ and $\mathcal{F}^{\square}$ become dense in each other, meaning that the chirality at large R disappears in a discontinuous way. Such a problem is not present in the one-dimensional case and, as shown in [20], all energy minima at large-R tend to fall smoothly on the limiting value $\omega = \omega^*$. If this interpretation is correct, then the chiral or achiral behavior of a discrete two-dimensional cylindrical ionic lattice should be relatively independent of the interaction potential, and similar results should hold also for two-dimensional lattices with short-range interactions. In Secs. IV A and IV B we test this hypothesis by considering (i) a simple model of a triangular network of elastic springs rolled around the cylinder and (ii) the effect of higher-order curvature corrections to this scenario.

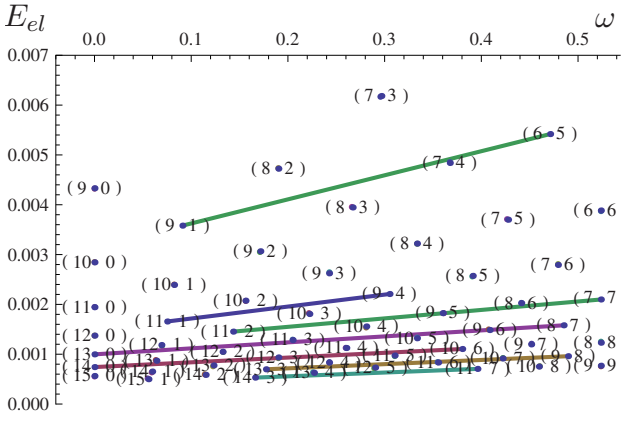

FIG. 8. (Color online) This figure shows a plot analogous to the ones in Figs. 5 and 6 but for a triangular lattice of particles interacting via purely elastic harmonic forces, with $l=1$. The plot is obtained for $k=100$ and for comparison the elastic energy of the lattice was calculated on per cell basis for the 2:1 charge ratio.

A. Adding elastic interactions

The fact that short-range interactions can induce chiral configurations in cylindrical geometries has been described in several numerical and theoretical works [4,43–45]. In this section we focus on a cylindrical lattice of particles that are interacting via short-range (nearest-neighbor) elastic forces. More precisely each particle on the triangular lattice is permanently connected to its six neighbors via harmonic springs, with spring constant k. The springs are massless and have length $l \geq 0$ for the sake of generality. The elastic energy per unit cell is

$$E_{el}(k) = \frac{k}{2} \sum_{\langle i,j \rangle} (D_{ij} - l)^2, \tag{16}$$

where D_{ij} is given in Eq. (9) and the sum is over all neighboring particles $\langle i,j \rangle$ per unit cell. The evaluation of the energy E_{el} is straightforward, and being local it does not require the Ewald summation method. The typical results are presented in Fig. 8, and show that short-range elastic interactions alone have a similar behavior to the one described in Sec. III. Furthermore, we repeated the calculations of this section both at finite l and $l=0$ and also for a repulsive-attractive Lennard-Jones potential. In all cases we found a behavior similar to the one in Fig. 8. The main difference between the elastic case and the case with Coulomb interactions is that for $0 \leq \omega \leq \pi/6$, E_{el} increases with ω in the 2:1 case (within a given family at fixed R), while it decreases with ω in the 1:1 and 3:1 case. This fact should not come as a surprise since the unit cells of the 2:1 case and 3:1 case are rotated of $\pi/6$ with respect to each other when considering the underlying triangular lattice of all charges, positive and negative. Since the elastic energy in Eq. (16) is independent from the charge distribution, one can anticipate that the behavior of E_{el} for the 3:1 case for $0 \leq \omega \leq \pi/6$ is equal to the behavior of E_{el} for the 2:1 case for $\pi/6 \leq \omega \leq \pi/3$ (hence the opposite slope). We can therefore focus on the 2:1 case, without loss of generality. In such a case, a positive slope means that the lowest-energy configuration is achiral $(p,0)$ for the class $\mathcal{F}^{\square}$ and chiral for the class $\mathcal{F}^{\diamond}$. This behavior is opposite to the one observed for long-range electrostatic forces in the 2:1 case. We therefore consider a model that combines the two effects, with an energy function $E_{total} = E_{cell} + E_{el}(k) = E_{cell} + kE_{el}(1)$. We use k as a control parameter for the relative strength of the elastic energy with respect to the electrostatic energy. Since E_{total} is a simple linear combination, its minimization is straightforward. We find that E_{total} presents an instability, which depends on the value of R. Namely, given a family of configurations that correspond to a given value of R, it is possible to fine tune k such that each one of the family member can be a minimum for E_{total}. However such a fine-tune procedure is R dependent, and the range of values of k for that to happen varies from family to family. The specific chiral indices and the number of members in each family have a number-theoretic nature and it is hard to extrapolate universal trends. Therefore, for the families we considered in this paper (see list in the Appendix section), we could not draw any general conclusion on the behavior of k with the radius R or with the chiral indices (p_1,p_2). The only systematic observation we can make is that for a generic values of k the scenario of Sec. III is not modified by adding short-range interactions. Achiral configurations dominate for most values of k, which one, whether (p,p) kind or $(p,0)$ kind, depends only on the relative strength of the long-range interaction versus the short-range interaction. This behavior is again different from what we observed in one-dimensional striped patterns on a cylinder, where even when including short-range interactions (such as line tension term), chiral configurations arise spontaneously and without any fine tune of the elastic forces.

It is interesting to note that in the 3:1 case the electrostatic energy and the elastic energy have negative slopes as a function of ω in the interval $0 \leq \omega \leq \pi/6$, and therefore the minima are always at the achiral zigzag configurations of type $(p,0)$ whenever possible. The same situation applies for the 1:1 case.

Despite of the different behaviors, in both the 2:1 and 3:1 cases the curvature of the cylinder has a crucial role in selecting achiral configurations of armchair or zigzag types for elastic forces (in the 2:1 or 3:1 case, respectively) and of zigzag type for electrostatics. In Sec. IV B we therefore include higher-order curvature effects in our model, such as the ones that arise by imposing a fixed three-dimensional bond-distance between nearest neighbors.

B. Adding higher-order curvature corrections

Higher-order curvature effects of cylindrical lattices are important at small values of the cylinder radius and have been considered in a number of papers (see, e.g., [46–48]). These effects take into account the more realistic situation where the charges fully pack the surface of the cylinder while the three-dimensional hard-core repulsion between neighbors does not glue them on the surface, so that they can distribute freely according to the cylinder curvature. The model we consider is an adaptation from Cox and Hill [46], where the authors described how one can keep three-dimensional bond lengths fixed on a hexagonal lattice rolled

TABLE I. Lattice parameters $\mathbf{a}_1$, $\mathbf{a}_2$, γ, ω.

Parameter	2:1	3:1
$\mathbf{a}_1$	$\mathbf{v}_1+\mathbf{v}_2$	$2\mathbf{v}_1$
$\mathbf{a}_2$	$2\mathbf{v}_2-\mathbf{v}_1$	$2\mathbf{v}_2$
γ	$\arccos\sqrt{\frac{1+\cos\Gamma}{10-8\cos\Gamma}}$	Γ
ω	$\arccos\frac{\cos(\Gamma-\Omega)+\cos\Omega}{\sqrt{2+2\cos\Gamma}}$	Ω

around a cylinder. This model still requires a pair of chiral indices (p_1,p_2) that define the orientation of the lattice. Any point P on the cylinder can be described by cylindrical coordinates $\{\psi,\beta\}$, such that $P(\psi,\beta)=R\cos\psi\hat{\mathbf{x}}+R\sin\psi\hat{\mathbf{y}}+R\beta\hat{\mathbf{z}}$. For convenience β measures z in units of R, and the origin is at $O=P(0,0)=R\hat{\mathbf{z}}$. Let the two lattice vectors be $A=P(\psi_1,\beta_1)$ and $B=P(\psi_2,\beta_2)$. The commensurability conditions are

$$p_1\psi_1+p_2\psi_2=2\pi, \quad p_1\beta_1+p_2\beta_2=0. \tag{17}$$

Moreover, the fixed-bond length condition requires the triangle $\Delta\mathbf{OAB}$ to be equilateral (for details see Ref. [46]),

$$\overline{\mathbf{OA}}=\overline{\mathbf{AB}}, \quad \overline{\mathbf{OA}}=\overline{\mathbf{OB}}. \tag{18}$$

The four unknown parameters ψ_1, ψ_2, β_1, β_2 that describe the lattice on the cylinder can be determined uniquely by solving the four equations [Eqs. (17) and (18)]. The solution defines a two-dimensional lattice with lattice vectors $\mathbf{v}_1$, $\mathbf{v}_2$, lattice angle Γ, and chiral angle Ω given by

$$\mathbf{v}_1=\{R\psi_1,R\beta_1\}, \quad \mathbf{v}_2=\{R\psi_2,R\beta_2\}, \tag{19}$$

$$\Gamma=\arccos\left(\frac{\mathbf{v}_1\cdot\mathbf{v}_2}{|\mathbf{v}_1||\mathbf{v}_2|}\right), \tag{20}$$

$$\Omega=\arccos\left(\frac{\mathbf{v}_1\cdot\hat{\mathbf{x}}}{|\mathbf{v}_1|}\right). \tag{21}$$

Such a lattice represents all possible positions of charges over the cylinder surface under the given constraints. We note that while the conditions [Eq. (18)] impose that $|\mathbf{v}_1|=|\mathbf{v}_2|$, the lattice is in general oblique and not triangular (i.e., $\Gamma\neq\pi/3$). Moreover, when considering different ionic ratios 2:1 and 3:1 while maintaining electroneutrality, it is once again convenient to use the sublattice of positive charges only, with lattice parameters $\mathbf{a}_1$, $\mathbf{a}_2$ lattice angle γ, and chiral angle ω. The relations among the parameters of the positive charge sublattice and the lattice of all possible positions are shown in Table I.

With the lattice parameters in hand we can now input them into E_{cell} in Eq. (12) and minimize the lattice energy with respect to ω. The minimization cannot be performed at fixed cylinder radius this time. The reason is that it is no longer possible to find two pairs of chiral indices that are degenerate. In order to compare the energies, we have to relax the condition of fixed radius and compare configurations that belong to cylinders with radii that differ from one another within a factor that we fix at 1%. The choice of such a cutoff is arbitrary, and different choices would lead to different results. Our main purpose here is to check whether chiral configurations can arise spontaneously by including higher-order curvature correction terms, at least qualitatively, and not to provide a complete classification and characterization of chiral and not chiral configurations for fixed-bond cylindrical lattices. Some typical values of the energies are shown in Table II. The situation is similar to the one described previously. We find chiral configuration only for families that include a zigzag (p,p) configuration, and otherwise the system prefers to be achiral with armchair $(p,0)$ configurations.

TABLE II. Chirality of 2:1 triangular lattices over a cylinder.

T	(p_1,p_2)	ω	E_{cell}	Chiral?
	(7,7)	$\pi/6$	−4.69	
147	(11,2)	0.151	−4.58	N
	(21,0)	0	−4.61	
441	(15,9)	0.39	−4.68	Y
	(13,13)	$\pi/6$	−4.70	
507	(22,1)	0.04	−4.60	N
	(14,14)	$\pi/6$	−4.70	
588	(22,4)	0.15	−4.57	N
	(33,0)	0	−4.61	
	(32,2)	0.05	−4.61	
1089	(22,16)	0.44	−4.71	Y

Because of this negative result, we decide therefore to not explore further this case. We considered different cutoff values and always found that at small radii higher-order curvature corrections do not change the above scenario as far as chiral configurations are concerned.

V. CONCLUSIONS

In this paper we considered a simple model for studying whether electrostatic interactions can induce chiral configurations of an ionic lattice wrapped around a cylinder. The motivation stems from a similar study [20] where a one-dimensional lattice of charged stripes on a cylinder prefers chiral configurations due to long-range electrostatics. We find that in the two-dimensional case the behavior is different. We find that the ionic lattice adopts achiral zigzag (p,p) configurations as long as the commensurability condition allows. In other words, at larger radii the lattice is able to choose from a grower set of configurations and tends to adopt the configuration which is as close as possible to a (p,p) configuration with $\omega=\pi/6$. We also observed that for families containing armchair $(p,0)$ configurations, the lowest energy is given by chiral configurations. As R increases the energetic differences between the families are attenuated by a power-law scaling as $\partial E_{cell}/\partial\omega\simeq R^{-4}$. This shows that although the electrostatic potential has a nonvanishing $1/R^2$ chiral term in the asymptotic $1/R$ expansion [20], such term is suppressed in E_{cell}. The double summation over the reciprocal space in Eq. (12) and the commensurability conditions

together destroy the instability that lead instead to spontaneous chiral configurations for one-dimensional striped patterns [20]. Changing the stoichiometric ratio, introducing elastic forces, or higher-order curvature corrections does not modify the situation very significantly. Therefore, we set forth the hypothesis that the main hindrance preventing spontaneous chirality of two-dimensional lattices is the commensurability constraint. That is, in the case of charged stripes wrapped around a cylinder the commensurability constraint has a one-parameter family of solutions, while the two-dimensional case has a discrete set of solutions (i.e., zero dimension). Thus, in the one-dimensional case the chiral angle and R can vary continuously, while in ionic lattices can only have discrete sets of chiral angles and fiber radii R. In the former case, the energy minimum coincides with the chiral minima of the Fourier transform of the electrostatic potential, while in the latter case that is not possible. A possible solution could be reintroduce a continuum degree of freedom on the two-dimensional ionic lattice, such as a unit cell that has some directionality (e.g., elliptic particles) or dipolar interactions. Our results do not exclude that other types of potentials might produce spontaneous chiral configurations. The Tersoff-Brenner potential is an example that includes empirical bond ordering [49], which is successfully used in describing covalently bonded carbon atoms of the graphene lattice of carbon nanotubes. Such a potential, while self-consistently describing a diverse set of bonded atoms, contains an anisotropic part that can be tuned to modulate the nanotube chirality [50]. However, in this work we limit to the study of isotropic interactions, and generalizations will be considered elsewhere. We note that the two-dimensional commensurability constraint may have consequences in systems where nanopatterns arise on cylindrical surfaces. For example, charged cationic-anionic lipids that coassemble into fibers can form nanopatterns of hexagonally arranged domains rich in one charged component due to competition between the repulsive charge accumulation and the short-range immiscibility [51], as well as lamellar patterns [20]. Achiral hexagonal nanopatterns were previously analyzed [51], and it was found that hexagonal domains discontinuously adopt lamellar patterns at small R due to the commensurability restriction, while a fiber with lamellar patterns can simply coarsen as R decreases satisfying commensurability automatically. Since in this paper we show that pure elastic interactions give only achiral configurations, we propose that the enhancement of lamellar patterns on cylinders will be observed in other nanostructures on cylindrical surfaces, such as those in incompatible alloys with competing strain (or stress) and a line tension forces [52] or lipids with competing interactions [53,54]. In other words, since the effective interactions change when the surface is curved, the equilibrium periodicities are a function of the radius R and they can shrink or coarsen depending on the nature of the interactions (even when keeping a constant solid angle per molecule). Further, the geometrical restrictions of a hexagonal lattice when folded onto a cylinder are difficult to satisfy for arbitrary periodicities without involving costly energetic defects, while a lamellar structure is preferred on the surface of cylinders because it has less constraints to accommodate arbitrary period structure, as described in Ref. [51], for the case of incompatible cationic-anionic molecules.

TABLE III. Zigzag families $\mathcal{F}^{\diamond}$ of triangular lattices for $T \leq 10^4$.

147	(7, 7), (11, 2)	4107	(37, 37), (47, 26)
507	(13, 13), (22, 1)	4332	(38, 38), (52, 22)
588	(14, 14), (22, 4)	4563	(39, 39), (66, 3)
1083	(19, 19), (26, 11)	5292	(42, 42), (66, 12)
1323	(21, 21), (33, 6)	5547	(43, 43), (61, 22)
2028	(26, 26), (44, 2)	7203	(49, 49), (71, 23), (77, 14)
2352	(28, 28), (44, 8)	8112	(52, 52), (88, 4)
2883	(31, 31), (46, 13)	9408	(56, 56), (88, 16)
3675	(35, 35), (55, 10)	9747	(57, 57), (78, 33)

It is important at this point to make some physical consideration. Our model is derived under the framework of an ionic lattice that is in thermodynamic equilibrium with an aqueous environment. We assume the counterions are condensed on the surface in order to screen the charge since here we assume no screening from the solution—a salt—free case. The effect of the curvature of the double layer over the cylinder's surface was neglected [55]. Further, the model does not consider the effect of counterion mediated polarization or short-range attractions due to neighboring charged rodlike polymers [56,57] and polyanionic assemblies such as DNA [58–60] and actin filaments [61,62]. Interestingly, the adsorption of polyelectrolytes on the surface of a charged nanofiber can lead to helical wrappings, which have been observed in numerous systems [63], and it was an area we

TABLE IV. Armchair families $\mathcal{F}^{\square}$ of triangular lattices for $T \leq 10^4$.

49	(5, 3), (7, 0)	3969	(45, 27), (63, 0)
169	(8, 7), (13, 0)	4225	(40, 35), (65, 0)
196	(10, 6), (14, 0)	4489	(45, 32), (67, 0)
361	(16, 5), (19, 0)	4900	(50, 30), (70, 0)
441	(15, 9), (21, 0)	5329	(63, 17), (73, 0)
676	(16, 14), (26, 0)	5476	(66, 14), (74, 0)
784	(20, 12), (28, 0)	5776	(64, 20), (76, 0)
961	(24, 11), (31, 0)	5929	(55, 33), (77, 0)
1225	(25, 15), (35, 0)	6084	(48, 42), (78, 0)
1369	(33, 7), (37, 0)	6241	(51, 40), (79, 0)
1444	(32, 10), (38, 0)	7056	(60, 36), (84, 0)
1521	(24, 21), (39, 0)	7396	(70, 26), (86, 0)
1764	(30, 18), (42, 0)	8281	(56, 49), (65, 39),
1849	(35, 13), (43, 0)		(80, 19), (85, 11), (91, 0)
2401	(35, 21), (39, 16), (49, 0)	8649	(72, 33), (93, 0)
2704	(32, 28), (52, 0)	9025	(80, 25), (95, 0)
3136	(40, 24), (56, 0)	9409	(57, 55), (97, 0)
3249	(48, 15), (57, 0)	9604	(70, 42), (78, 32)
3721	(56, 9), (61, 0)		(98, 0)
3844	(48, 22), (62, 0)		

TABLE V. Armchair families of square lattices for $T \leq 10^4$.

25	(4, 3), (5, 0)	3600	(48, 36), (60, 0)
100	(8, 6), (10, 0)	3721	(60, 11), (61, 0)
169	(12, 5), (13, 0)	4225	(52, 39), (56, 33),
225	(12, 9), (15, 0)		(60, 25), (63, 16), (65, 0)
289	(15, 8), (17, 0)	4624	(60, 32), (68, 0)
400	(16, 12), (20, 0)	4900	(56, 42), (70, 0)
625	(20, 15), (24, 7), (25, 0)	5329	(55, 48), (73, 0)
676	(24, 10), (26, 0)	5476	(70, 24), (74, 0)
841	(21, 20), (29, 0)	5625	(60, 45), (72, 21), (75, 0)
900	(24, 18), (30, 0)	6084	(72, 30), (78, 0)
1156	(30, 16), (34, 0)	6400	(64, 48), (80, 0)
1225	(28, 21), (35, 0)	6724	(80, 18), (82, 0)
1369	(35, 12), (37, 0)	7225	(68, 51), (75, 40),
1521	(36, 15), (39, 0)		(77, 36), (84, 13), (85, 0)
1600	(32, 24), (40, 0)	7569	(63, 60), (87, 0)
1681	(40, 9), (41, 0)	7921	(80, 39), (89, 0)
2025	(36, 27), (45, 0)	8100	(72, 54), (90, 0)
2500	(40, 30), (48, 14), (50, 0)	8281	(84, 35), (91, 0)
2601	(45, 24), (51, 0)	9025	(76, 57), (95, 0)
2704	(48, 20), (52, 0)	9409	(72, 65), (97, 0)
2809	(45, 28), (53, 0)	10000	(80, 60), (96, 28),
3025	(44, 33), (55, 0)		(100, 0)
3364	(42, 40), (58, 0)		

TABLE VI. Zigzag families of square lattices for $T \leq 10^4$.

50	(5, 5), (7, 1)	3200	(40, 40), (56, 8)
200	(10, 10), (14, 2)	3362	(41, 41), (49, 31)
338	(13, 13), (17, 7)	4050	(45, 45), (63, 9)
450	(15, 15), (21, 3)	5000	(50, 50), (62, 34), (70, 10)
578	(17, 17), (23, 7)	5202	(51, 51), (69, 21)
800	(20, 20), (28, 4)	5408	(52, 52), (68, 28)
1250	(25, 25), (31, 17), (35, 5)	5618	(53, 53), (73, 17)
1352	(26, 26), (34, 14)	6050	(55, 55), (77, 11)
1682	(29, 29), (41, 1)	6728	(58, 58), (82, 2)
1800	(30, 30), (42, 6)	7200	(60, 60), (84, 12)
2312	(34, 34), (46, 14)	7442	(61, 61), (71, 49)
2450	(35, 35), (49, 7)	8450	(65, 65), (79, 47),
2738	(37, 37), (47, 23)		(85, 35), (89, 23), (91, 13)
3042	(39, 39), (51, 21)	9248	(68, 68), (92, 28)
		9800	(70, 70), (98, 14)

considered in a previous work [30]. The model is defined under the condition that the inverse screening length is very short compared with the inverse bond length. While for lamellar patterns in Refs. [20,30] the screening length is the controlling the length scale, our focus in this paper is with the minimization of the energy with the lattice orientation. Moreover the lattice is chosen with an equal-length lattice vectors, such that no direction had a preselected asymmetry assigned to it. Our model can be extended to include other Bravais lattices and charge stoichiometric ratios. An even more interesting generalization would be to consider a unit-cell charge distribution that interpolates between circular domains and elongated directional (e.g., elliptical) domains, thereby locating the crossover point from the two-dimensional achiral ionic lattices and the one-dimensional helical ones, solely due to the Coulomb electrostatic potential. We postpone this discussion to a future publication.

ACKNOWLEDGMENTS

The authors acknowledge the support of the NSF Grant No. DMR 0907781 for its financial support. K.L.K. wishes to thank the Krell Institute for their support with the CSGF Award No. DE-FG02-97ER2530 from the Department of Energy and the Nanoscale Science and Engineering Initiative by the National Science Foundation under Award No. EEC-0647560 for partial support.

APPENDIX

In this appendix we report Tables III–VI with degenerate families for the triangular lattice (where $T=p_1^2+p_2^2+p_1p_2$) and the square lattice (where $T=p_1^2+p_2^2$). In both cases, the families are separated in two classes: the armchair families $\mathcal{F}^{\square}$ and the zigzag families $\mathcal{F}^{\diamond}$. We reiterate that here we list only the pairs of chiral indices (p_1,p_2) with $p_1 \geq p_2$ because the electrostatic energy of any (p_1,p_2) configuration is the same of the corresponding (p_2,p_1) configuration.

[1] J. M. McBride and J. C. Tully, Nature (London) **452**, 161 (2008).
[2] J. B. S. Haldane, Nature (London) **185**, 87 (1960).
[3] L. Pasteur, C.R. Acad. Sci. Paris **78**, 1515 (1874).
[4] A. Aggeli, I. A. Nyrkova, M. Bell, R. Harding, L. Carrick, T. C. B. McLeish, A. N. Semenov, and N. Boden, Proc. Natl. Acad. Sci. U.S.A. **98**, 11857 (2001).
[5] D. A. Marvin, L. C. Welsh, M. F. Symmons, W. R. P. Scott, and S. K. Straus, J. Mol. Biol. **355**, 294 (2006).
[6] D. S. Thiriot, A. A. Nevzorov, and S. J. Opella, Protein Sci. **14**, 1064 (2005).
[7] X. D. Yan, N. H. Olson, J. L. Van Etten, M. Bergoin, M. G. Rossmann, and T. S. Baker, Nat. Struct. Biol. **7**, 101 (2000).
[8] R. Keller, Development **133**, 2291 (2006).
[9] F. Z. Jiang, H. Horber, J. Howard, and D. J. Muller, J. Struct. Biol. **148**, 268 (2004).
[10] C. Valéry, M. Paternostre, B. Robert, T. Gulik-Krzywicki, T. Narayanan, J. C. Dedieu, G. Keller, M. L. Torres, R. Cherif-Cheikh, P. Calvo, and F. Artzner, Proc. Natl. Acad. Sci. U.S.A. **100**, 10258 (2003).
[11] J. Zhang, M. T. Albelda, Y. Liu, and J. W. Canary, Chirality **17**, 404 (2005).

[12] L. S. Li, H. Z. Jiang, B. W. Messmore, S. R. Bull, and S. I. Stupp, Angew. Chem., Int. Ed. **46**, 5873 (2007).
[13] S. Zhong, H. G. Cui, Z. Y. Chen, K. L. Wooley, and D. J. Pochan, Soft Matter **4**, 90 (2008).
[14] T. Oda, K. Makino, I. Yamashita, K. Namba, and Y. Maeda, Biophys. J. **80**, 841 (2001).
[15] V. A. Belyi and M. Muthukumar, Proc. Natl. Acad. Sci. U.S.A. **103**, 17174 (2006).
[16] B. Tarus, J. E. Straub, and D. Thirumalai, J. Mol. Biol. **379**, 815 (2008).
[17] G. Vernizzi and M. O. de la Cruz, Proc. Natl. Acad. Sci. U.S.A. **104**, 18382 (2007).
[18] M. Dubois, B. Deme, T. Gulik-Krzywicki, J. C. Dedieu, C. Vautrin, S. Desert, E. Perez, and T. Zemb, Nature (London) **411**, 672 (2001).
[19] S. De Feyter and F. C. De Schryver, Chem. Soc. Rev. **32**, 139 (2003).
[20] K. L. Kohlstedt, F. J. Solis, G. Vernizzi, and M. O. de la Cruz, Phys. Rev. Lett. **99**, 030602 (2007).
[21] H. Liang, D. Harries, and G. C. L. Wong, Proc. Natl. Acad. Sci. U.S.A. **102**, 11173 (2005).
[22] S. T. Hess, M. Kumar, A. Verma, J. Farrington, A. Kenworthy, and J. Zimmerberg, J. Cell Biol. **169**, 965 (2005).
[23] M. Edidin, Trends Cell Biol. **11**, 492 (2001).
[24] A. A. Kornyshev, D. J. Lee, S. Leikin, and A. Wynveen, Rev. Mod. Phys. **79**, 943 (2007).
[25] M. Kanduč, J. Dobnikar, and R. Podgornik, Soft Matter **5**, 868 (2009).
[26] K. Andresen, R. Das, H. Y. Park, H. Smith, L. W. Kwok, J. S. Lamb, E. J. Kirkland, D. Herschlag, K. D. Finkelstein, and L. Pollack, Phys. Rev. Lett. **93**, 248103 (2004); V. B. Chu, Y. Bai, J. Lipfert, D. Herschlag, and S. Doniach, Biophys. J. **93**, 3202 (2007).
[27] K. Rajangam, H. A. Behanna, M. J. Hui, X. Q. Han, J. F. Hulvat, J. W. Lomasney, and S. I. Stupp, Nano Lett. **6**, 2086 (2006).
[28] J. F. Campbell, I. Tessmer, H. H. Thorp, and D. A. Erie, J. Am. Chem. Soc. **130**, 10648 (2008).
[29] K. L. Niece, J. D. Hartgerink, J. Donners, and S. I. Stupp, J. Am. Chem. Soc. **125**, 7146 (2003).
[30] G. Vernizzi, K. L. Kohlstedt, and M. Olvera de la Cruz, Soft Matter **5**, 736 (2009).
[31] M. S. Dresselhaus, G. Dresselhaus, A. Jorio, A. G. Souza, and R. Saito, Carbon **40**, 2043 (2002).
[32] E. B. Barros, A. Jorio, G. G. Samsonidze, R. B. Capaz, A. G. Souza, J. Mendes, G. Dresselhaus, and M. S. Dresselhaus, Phys. Rep. **431**, 261 (2006).
[33] M. J. Bowick, A. Cacciuto, D. R. Nelson, and A. Travesset, Phys. Rev. B **73**, 024115 (2006).
[34] D. Vanderbilt, *Proceedings of the Fifth International Conference on the Structure of Surfaces (ICSOS-5)* (World Scientific, Aix Provence, 1996), p. 811.
[35] B. W. Wessels, *Proceedings of the 24th Annual Conference on the Physics and Chemistry of Semiconductor Interfaces (PCSI-24)* (American Institute of Physics, Res Triangle Park, NC, 1997), p. 1056.
[36] J. M. García, J. P. Silveira, and F. Briones, Appl. Phys. Lett. **77**, 409 (2000).
[37] O. Hellwig, A. Berger, and E. E. Fullerton, Phys. Rev. Lett. **91**, 197203 (2003).
[38] T. P. Russell, Curr. Opin. Colloid Interface Sci. **1**, 107 (1996).
[39] K. Binder, *Polymers in Confined Environments* (Springer-Verlag, Berlin, 1999), p. 1.
[40] J.-C. Charlier and J.-P. Issi, Appl. Phys. A: Mater. Sci. Process. **67**, 79 (1998).
[41] P. P. Ewald, Ann. Phys. **64**, 253 (1921).
[42] G. Hummer, Chem. Phys. Lett. **235**, 297 (1995).
[43] R. L. B. Selinger, J. V. Selinger, A. P. Malanoski, and J. M. Schnur, Phys. Rev. Lett. **93**, 158103 (2004).
[44] G. T. Pickett, M. Gross, and H. Okuyama, Phys. Rev. Lett. **85**, 3652 (2000).
[45] J. V. Selinger, F. C. MacKintosh, and J. M. Schnur, Phys. Rev. E **53**, 3804 (1996).
[46] B. J. Cox and J. M. Hill, Carbon **45**, 1453 (2007).
[47] V. N. Popov, New J. Phys. **6**, 17 (2004).
[48] G. G. Samsonidze, R. Saito, N. Kobayashi, A. Grüneis, J. Jiang, A. Jorio, S. G. Chou, G. Dresselhaus, and M. S. Dresselhaus, Appl. Phys. Lett. **85**, 5703 (2004).
[49] D. W. Brenner, Phys. Rev. B **42**, 9458 (1990).
[50] S. R. Phillpot and S. B. Sinnott, Science **325**, 1634 (2009).
[51] F. J. Solis, S. I. Stupp, and M. O. de la Cruz, J. Chem. Phys. **122**, 054905 (2005).
[52] O. L. Alerhand, D. Vanderbilt, R. D. Meade, and J. D. Joannopoulos, Phys. Rev. Lett. **61**, 1973 (1988).
[53] M. Seul and D. Andelman, Science **267**, 476 (1995).
[54] C. Singh, P. K. Ghorai, M. A. Horsch, A. M. Jackson, R. G. Larson, F. Stellacci, and S. C. Glotzer, Phys. Rev. Lett. **99**, 226106 (2007).
[55] B. Duplantier, R. E. Goldstein, V. Romero-Rochin, and A. I. Pesci, Phys. Rev. Lett. **65**, 508 (1990).
[56] F. J. Solis and M. O. de la Cruz, Phys. Rev. E **60**, 4496 (1999).
[57] T. E. Angelini, R. Golestanian, R. H. Coridan, J. C. Butler, A. Beraud, M. Krisch, H. Sinn, K. S. Schweizer, and G. C. L. Wong, Proc. Natl. Acad. Sci. U.S.A. **103**, 7962 (2006).
[58] L. Dai, Y. G. Mu, L. Nordenskiöld, and J. R. C. van der Maarel, Phys. Rev. Lett. **100**, 118301 (2008).
[59] E. Raspaud, D. Durand, and F. Livolant, Biophys. J. **88**, 392 (2005).
[60] E. Raspaud, M. O. de la Cruz, J. L. Sikorov, and F. Livolant, Biophys. J. **74**, 381 (1998).
[61] T. E. Angelini, H. Liang, W. Wriggers, and G. C. L. Wong, Eur. Phys. J. E **16**, 389 (2005).
[62] L. K. Sanders, C. Guáqueta, T. E. Angelini, J. W. Lee, S. C. Slimmer, E. Luijten, and G. C. L. Wong, Phys. Rev. Lett. **95**, 108302 (2005).
[63] D. A. Marvin, Int. J. Biol. Macromol. **11**, 159 (1989).